Nano Research

Open Access

Research Article

Intermittent pulsed electrocatalysis adjusting Cu valence states for effective nitrite reduction to ammonia

Zhe Meng[1,§], Jian-Hui Yi[1,§], Yu-Tian Zhang[1], Xue-Feng Sun[1], Xiao-Lei Huang[2] ✉, Miao-Miao Shi[1], Fei-Fei Zhang[1], Jun-Min Yan[1] ✉, and Qing Jiang[1]

[1] *Key Laboratory of Automobile Materials, Ministry of Education, School of Materials Science and Engineering, Jilin University, Changchun 130022, China*
[2] *Key Laboratory of Rare Earths, Ganjiang Innovation Academy, Chinese Academy of Sciences, Ganzhou 341000, China*
[§] *Zhe Meng and Jian-Hui Yi contributed equally to this work.*

Cite this article: *Nano Research*, **2025**, *18*, 94907810. https://doi.org/10.26599/NR.2025.94907810

ABSTRACT: Electrochemical nitrite (NO_2^-) reduction offers a sustainable route for ammonia (NH_3) synthesis while simultaneously removing contaminants in wastewater. However, its efficiency is often limited by low catalytic efficiency and the competitive hydrogen evolution reaction at low NO_2^- concentrations. Herein, we report an intermittent pulsed electrolysis (IPE) strategy using copper oxide (Cu_xO) nanowires, which significantly enhances the NH_3 yield rate and Faradaic efficiency (FE) at lower reactant concentrations. *In situ* experiments and theoretical calculations reveal that alternating between open-circuit and cathodic potentials modulates the copper oxidation states, stabilizing the catalytically active cuprous oxide (Cu_2O). Consequently, the IPE approach provides an outstanding NH_3 yield rate of 115.10 mg·h^{-1}·cm^{-2} and FE of 91.14% in the presence of 25 mM NO_2^-, markedly outperforming conventional constant potential electrolysis.

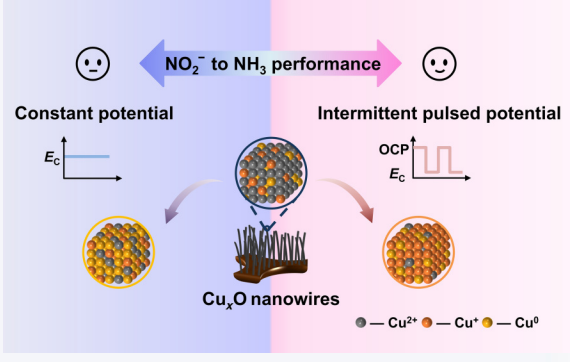

KEYWORDS: electrochemical nitrite reduction, ammonia synthesis, intermittent pulsed electrolysis, Cu_xO nanowires, stable cuprous oxide

1 Introduction

Ammonia (NH_3) plays a crucial role in modern society due to its extensive applications in agriculture, medicine, and industry, as well as its potential as a clean energy carrier [1, 2]. Industrial NH_3 synthesis primarily relies on the Haber–Bosch process [3], which operates under energy-intensive conditions and contributes significantly to carbon dioxide emissions [4–7]. As an alternative nitrogen source, nitrite (NO_2^-) is highly soluble and possesses a relatively low N=O bond dissociation energy, making it an attractive candidate for sustainable NH_3 production [8–11]. Thus, the electrochemical nitrite reduction reaction (eNO_2RR) offers a dual advantage: removing NO_2^- contaminants from wastewater while efficiently generating NH_3. Recent studies have demonstrated the feasibility of eNO_2RR using various catalysts, particularly for high NO_2^- concentrations (≥ 100 mM) [12–16]. While the high concentration scenarios typically occur in specialized contexts such as nuclear wastewater [16]. Most industrial effluents including tannery, food processing, and electroplating streams contain moderate NO_2^- concentrations (5–100 mM), where the hydrogen evolution reaction (HER) competition intensifies [17–19]. Therefore, producing NH_3 with high selectivity at lower NO_2^- concentrations remains a challenge.

Copper (Cu) is a common candidate for NO_x^- reduction reaction due to its unique $3d^{10}$ orbital and various valence states, which facilitates reactants coordination and adsorption [20–24]. Moreover, Cu-based tandem catalysts have been widely investigated due to the unique structure and stepwise reaction at dual-active sites [25–27]. Particularly, the reported CuO undergoes *in situ* transformation to Cu/Cu_2O after electrolysis. This Cu/Cu_2O interface significantly enhances the eNO_2RR activity, achieving a high Faradaic efficiency (FE) of 95.8% for NH_3 synthesis [28]. The enhanced performance is attributed to electron transfer from Cu_2O to Cu at the interface, which promotes the formation of *NOH

Received: April 29, 2025; **Revised:** July 11, 2025
Accepted: July 15, 2025

✉Address correspondence to Xiao-Lei Huang, xlhuang@gia.cas.cn; Jun-Min Yan, junminyan@jlu.edu.cn

intermediate and suppresses the HER. However, the individual contributions of Cu, Cu_2O, and CuO to NH_3 synthesis remain underexplored [29]. A major challenge is that Cu oxides are sensitive to potential fluctuations and environmental conditions, leading to catalyst instability [30]. Therefore, the main concern is to maintain more favorable Cu active sites throughout the long-term eNO_2RR process. Pulsed electrolysis has emerged as an effective method to enhance catalyst performance. By periodically modulating the applied potential, it can suppress competing reactions and prevent intermediate accumulation [31, 32]. Specifically, introducing periodic anodic potentials can regenerate the catalyst surface and modulate the oxidation state of Cu-based materials [33, 34]. Nevertheless, the use of an anodic potential increases overall power consumption, therefore, necessitating the exploration of simpler and more energy-efficient modulation techniques.

Herein, we investigate the intermittent pulsed electrolysis (IPE) technique to enhance eNO_2RR performance using *in situ* grown Cu_xO nanowires (NWs) on three-dimensional (3D) porous Cu foam at low concentrations (Scheme 1). The IPE technique alternates between open circuit potential (OCP) and cathodic potential (E_c), promoting the control formation of Cu_2O within Cu_xO. In contrast, conventional constant potential electrolysis (CE) favors the formation of Cu^0, which is less effective for eNO_2RR. Among three possible catalysts of CuO, Cu_2O, and Cu, density functional theory (DFT) calculations indicate that the Cu_2O (111) surface exhibits the strongest adsorption energy for NO_2^- and a negative free energy change for each electron transfer step in eNO_2RR. Therefore, the IPE mode approach enhances the Cu_2O content in Cu_xO, significantly optimizing catalytic activity. This strategy achieves an outstanding NH_3 yield rate of 115.10 $mg \cdot h^{-1} \cdot cm^{-2}$ and a FE of 91.14% at a high current density (> 1 $A \cdot cm^{-2}$), even in a low NO_2^- concentration of 25 mM.

2 Experimental

2.1 Chemicals and materials

Sodium hydroxide (NaOH, Sinopharm Chemical Reagent Co., Ltd, 96%), copper foam (Cu, Suzhou Keshenghe Metallic Materials Co., Ltd, 99.9%), ethanol (C_2H_5OH, Beijing Chemical Works, ≥ 99.7%), ammonium chloride (NH_4Cl, Sinopharm Chemical Reagent Co., Ltd, analytically reagent), hydrochloric acid (HCl, XiLong Scientific, A0300003, 36.0%–38.0%), sodium nitrite ($NaNO_2$, Aladdin, ≥ 99.0%), sodium citrate dihydrate ($C_6H_5Na_3O_7 \cdot 2H_2O$, Sinopharm Chemical Reagent Co., Ltd, analytically reagent), sodium nitroferricyanide dihydrate ($C_5FeN_6Na_2O \cdot 2H_2O$, Aladdin, 99%), sodium hypochlorite solution (NaClO, Aladdin, available chlorine 6.0%–14.0%), salicylic acid ($C_7H_6O_3$, Aladdin, 99.5%), N-(1-naphthyl)ethylendeiamine dihydrochioride ($C_{12}H_{14}N_2 \cdot 2HCl$, Aladdin, 98%), sulfanilamide ($C_6H_8N_2O_2S$, Aladdin, ≥ 99%), anion-exchange membrane (Alkrane-1; thickness: 0.06 ± 0.005 mm, ionic conductivity: 80 ± 10 $mS \cdot cm^{-1}$; provided by University of Science and Technology of China), and deionized water (SIEMENS, 18.2 MΩ·cm) were obtained commercially and used without further purified.

2.2 Synthesis of Cu_xO NWs catalysts

Cu_xO NWs were prepared in two steps including electrochemical anodization and thermal annealing methods. Cu foam was required to be pre-treated prior to anodization. To begin, the Cu foam was submerged in an HCl (1.0 M) aqueous solution for 5 min to dissolve the surficial oxides. Following that, it was cleaned sequentially with H_2O and C_2H_5OH and dried at 40 °C under vacuum. For the first anodization step, Cu foam was exposed to 30 $mA \cdot cm^{-2}$ in NaOH (3 M, 30 mL) electrolyte for 20 min, enabling *in situ* generation of blue $Cu(OH)_2$ NWs. For the second step, Cu_xO NWs catalysts were synthesized by annealing the sample in air at 300 °C for 2 h with 5 $°C \cdot min^{-1}$.

3 Results and discussion

Cu_xO NWs are synthesized in two steps including *in situ* anodic oxidation followed by annealing (Fig. 1(a) and Fig. S1 in the Electronic Supplementary Material (ESM)). The X-ray diffraction (XRD) pattern indicates the mixed phases of Cu_2O [21], CuO [35], and metallic Cu [28] in Cu_xO NWs (Fig. 1(b)). Scanning electron microscopy (SEM) analysis reveals that numerous straight Cu_xO NWs are uniformly grown on Cu foam (Figs. 1(c) and 1(d)). Meanwhile, Cu and O elements are uniformly dispersed in these NWs, as evidenced by energy dispersive X-ray spectrometry mapping (Fig. S2 in the ESM). The outwardly extended dense arrays of Cu_xO NWs facilitate the adequate exposure of the catalyst to the electrolyte and increase the contact areas between reactants and active sites. The transmission electron microscopy (TEM) image (Fig. 1(e)) verifies that the surfaces of Cu_xO NWs are comparatively flat and smooth. The high-resolution high-angle annular dark-field scanning TEM (HAADF-STEM) image shows the lattice spacings of 0.232 and 0.254 nm, corresponding to CuO (111) and (002) [20, 36], respectively. Furthermore, the filtered fast Fourier transformation (FFT) pattern of the correlation region provides [$1\bar{1}0$] zone axis information (Figs. 1(f) and 1(g)), consistent with the standard CuO crystal structure simulated along the same [$\bar{1}10$] zone axis (Fig. S3 in the ESM). This confirms that the main phase in Cu_xO NWs is the crystalline monoclinic CuO.

DFT calculations are conducted to discover the electronic

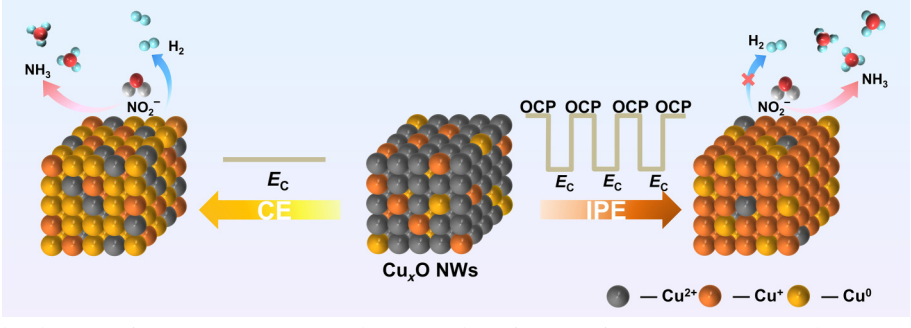

Scheme 1 Illustration for the adjustment of $Cu^{\delta+}$ species composition and improving the performance of eNO_2RR over Cu_xO NWs by IPE strategy.

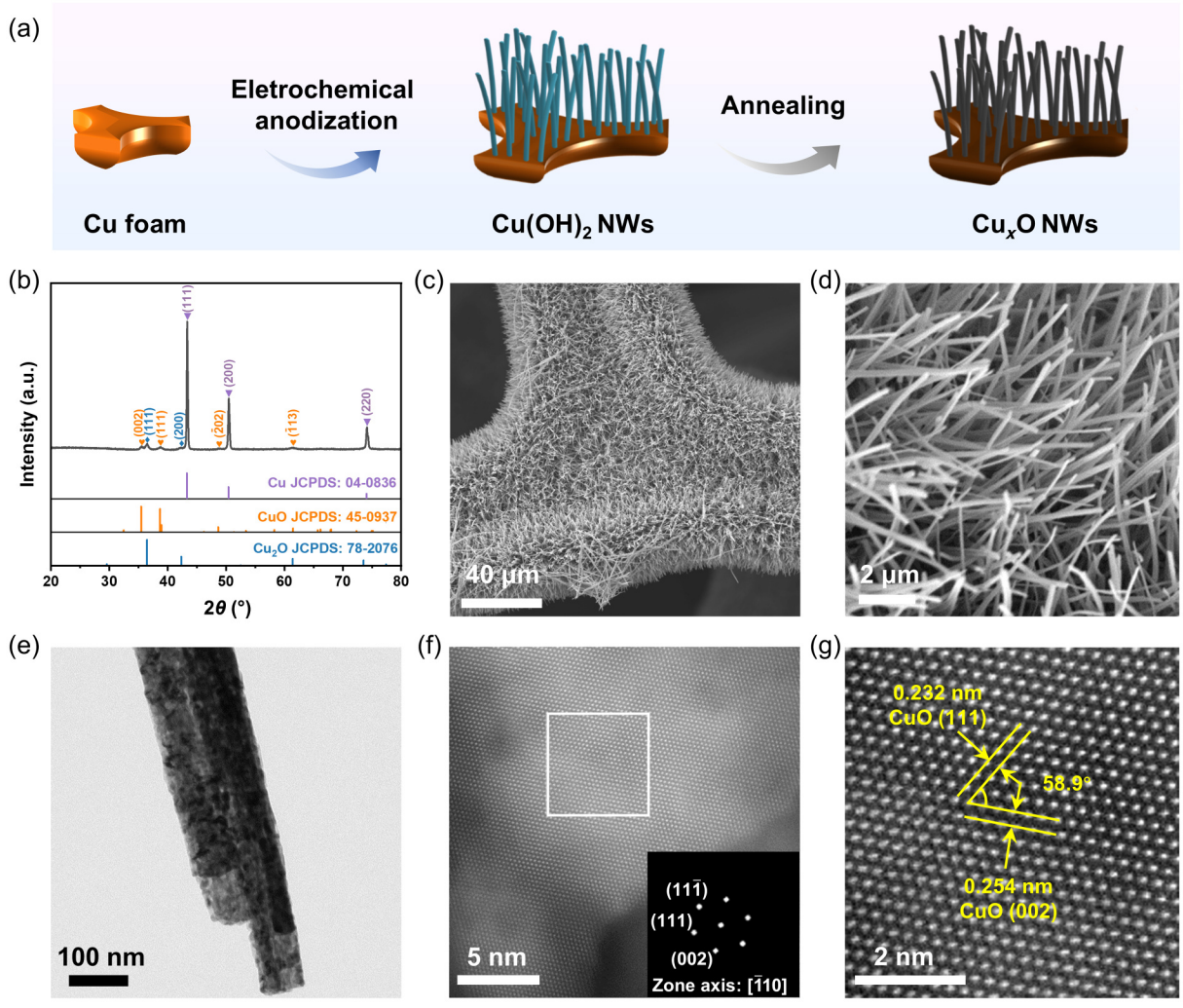

Figure 1 (a) Schematic illustration of the preparation of Cu_xO NWs. (b) XRD pattern of Cu_xO NWs on Cu foam. (c) and (d) SEM images, (e) TEM image, and (f) HAADF-STEM image of Cu_xO NWs. Inset: corresponding filtered FFT pattern. (g) The details of white-squared regions in (f).

structures and reaction mechanisms over CuO, Cu_2O, and Cu for eNO_2RR process, aiming to identify the most favorable active phases in Cu_xO NWs. The optimized Cu_2O (111), CuO (111) and Cu (111) planes are selected as the structural models according to XRD pattern (Fig. S4 in the ESM and Fig. 1(b)). Figure 2(a) displays the Gibbs free energy change (ΔG) profiles on Cu_2O (111), CuO (111) and Cu (111) for the reduction of NO_2^- to NH_3. The corresponding reaction intermediates are shown in Fig. S5 in the ESM. The rate-determining step (RDS) of the CuO surface is the hydrogenation of NO* to HNO* with ΔG of 0.31 eV, while the RDS of the Cu surface corresponds to the hydrogenation of NO_2* to NO_2H* with ΔG of 0.40 eV. However, the ΔG of these two steps are both reduced on the Cu_2O surface (−0.22 and −0.13 eV, respectively). Furthermore, the consistently negative ΔG values for all reaction steps on Cu_2O indicate that each electron-transfer step is exothermic, making Cu_2O the most favorable phase for eNO_2RR.

The adsorption properties of NO_2^- on Cu_2O, CuO, and Cu are also calculated. Cu atoms serve as the active sites, and NO_2^- tends to be adsorbed toward the Cu–Cu bridge sites. The adsorption energies of NO_2^- on Cu_2O, CuO, and Cu surfaces are −1.16, −0.49, and −0.78 eV, respectively. Consequently, Cu_2O can effectively adsorb and activate NO_2^-, which is conducive to the subsequent reaction steps. Moreover, the charge density difference (CDD) and Hirshfeld charge analysis also indicate the stronger interaction of NO_2^- with Cu_2O (Fig. 2(b)). Based on the partial density of states (PDOS), the d-band centers (ε_d) of Cu atoms on the surfaces of Cu_2O, CuO and Cu are calculated to be −1.84, −2.37, and −2.54 eV, respectively (Fig. 2(c)) [37]. The higher ε_d of Cu_2O indicates its stronger adsorption capability and interaction with adsorbates. Therefore, the strengthened binding of NO_2^- to the Cu_2O surface will contribute to enhanced eNO_2RR performance.

HER is the primary side reaction of eNO_2RR, resulting in a low FE due to the consumption of protons and electrons [17]. The ΔG of hydrogen adsorption (ΔG_{H^*}) on the catalyst surfaces is calculated (Fig. 2(d)). The results suggest that Cu_2O (ΔG_{H^*} = 0.32 eV) exhibits inferior performance in HER compared to Cu (ΔG_{H^*} = 0.08 eV). Additionally, the adsorption of NO_2^- is stronger than that of H_2O on the Cu_2O (Fig. S6 in the ESM). The results illustrate that the preferential adsorption of NO_2^- and inhibition of HER on Cu_2O leads to favorable catalytic activity and selectivity for NH_3 synthesis.

To stabilize the highly active Cu^+ and prevent its accelerated reduction to Cu^0 at negative reduction potentials [38], the IPE is implemented during eNO_2RR to generate more favorable active sites of Cu_2O via periodic oscillations between OCP and E_c [39]. To verify the feasibility of the IPE strategy, different Cu_xO NWs are characterized: (i) Cu_xO NWs after CE at −0.7 V (all potentials in

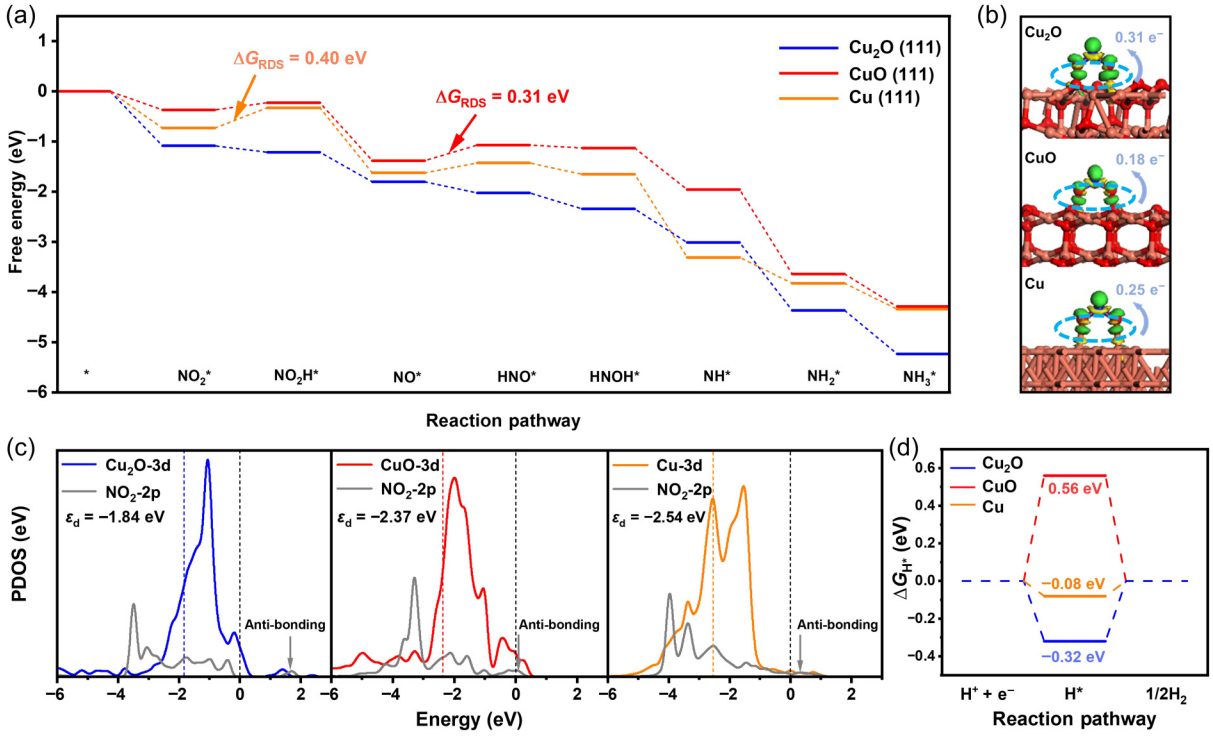

Figure 2 (a) ΔG profile of eNO_2RR on the surfaces of Cu_2O (111), CuO (111), and Cu (111). (b) CDD for NO_2^- adsorption on the surfaces of Cu_2O, CuO, and Cu. The yellow and the green isosurfaces represent charge depletion and accumulation, respectively. (c) PDOS of Cu-3d and NO_2-2p states on the surfaces of Cu_2O, CuO, and Cu. (d) ΔG_{H^*} diagrams of HER on different models.

this work are vs. RHE) for 30 min (Cu_xO NWs-C), and (ii) Cu_xO NWs after IPE with pulsed width (t_c) of 1 s and open-circuit rest time (t_r) of 1 s under E_c of −0.7 V for 30 min (Cu_xO NWs-I). Both the electrolyte is 1 M NaOH with 25 mM NO_2^-. As shown in the HAADF-STEM image (Fig. 3(a)), Cu_xO NWs-C exhibit lattice spacings of 0.211 and 0.180 nm, corresponding to Cu (111) and (200), respectively. The atomic structure and filtered FFT plots along the [0$\bar{1}$1] zone axis reveal the existence of metallic Cu (Fig. S7 in the ESM) [40]. That is, a part of CuO is reduced to metallic Cu during the CE. By contrast, Cu_2O is formed in Cu_xO NWs-I, which is identified by the existence of Cu_2O (111) and (200) with lattice spacings of 0.249 and 0.215 nm, respectively (Fig. 3(b) and Fig. S8 in the ESM) [41].

To further investigate the formation of Cu_2O in the IPE mode during eNO_2RR in 25 mM of NO_2^-, We first examined the potential dependence of the catalyst redox behaviour using *in situ* Raman spectroscopy (Fig. S9 in the ESM). The spectrum of the initial Cu_xO NWs exhibits the characteristic peaks of CuO (292 and 625 cm^{-1}) [42, 43] and Cu_2O (215 cm^{-1}) [28]. This observation confirms the mixed phases previously identified in XRD analysis (Fig. 1(b)), which detected a coexistence of metallic Cu, Cu_2O, and CuO. Besides, a weak peak at 113 cm^{-1} indicates the existence of an intermediate state between Cu_2O and Cu [44]. Upon applying increasingly negative potentials, the characteristic oxidation peaks intensity progressively diminishes and eventually disappears. Crucially, when return to OCP, the oxidation peaks rapidly reappear. This observation confirms that the spontaneous re-oxidation of Cu at OCP is a fundamental process underpinning the regeneration mechanism to the IPE mode. Furthermore, based on the trends observed in Fig. S9 in the ESM, a moderate E_c of −0.5 V provides a more stable window to probe the catalyst state evolution under IPE while preventing the undetectable signals caused by the rapid reduction of $Cu^{\delta+}$ species (Fig. 3(c)). Applying E_c for 30 s, the peak intensity of CuO decreases slightly accompanied by a little increase in that of Cu_2O. When prolonging E_c time up to 60 s, the peaks corresponding to $Cu^{\delta+}$ species become imperceptible, suggesting that metallic Cu serves as the actual active site under sustained negative potential. Once switching the potential from E_c to OCP for 30 s, the obvious Cu_2O signal reappears, indicating some Cu^0 atoms are rapidly oxidized to Cu^+. The peak at ~ 412 cm^{-1} of Cu_2O is attributed to the multiphonon process [45]. In addition, the peak at 570 cm^{-1} is probably caused by an intermediate in the early stage of Cu_2O formation [46, 47]. Therefore, the intermittent pulsed potential-controlled reduction and re-oxidation processes successfully revive the high activity of Cu_xO by regenerating Cu_2O. Further extending the OCP time to 90 s results in a slight increase in the CuO peaks intensities due to further oxidation. Thus, it is crucial to employ an appropriate IPE mode with proper E_c and OCP time to maximize the Cu_2O content and optimize catalyst performance.

X-ray photoelectron spectroscopy (XPS) is conducted to investigate the surface chemical states evolution of the as-prepared Cu_xO NWs, Cu_xO NWs-C, and Cu_xO NWs-I (Fig. 3(d)). For Cu_xO NWs, prominent peaks at binding energies of approximately 932.5 and 933.5 eV correspond to Cu^0/Cu^+ and Cu^{2+}, respectively [48, 49]. Whereas, the signals of Cu^{2+} decrease to negligible levels in Cu_xO NWs-C and Cu_xO NWs-I, which proves that Cu^{2+} is electrochemically reduced to Cu^0/Cu^+ during the treatment. And the intensity of the peak at about 531.5 eV in O 1s XPS spectra belonging to the adsorbed oxygen (O_A) [13] shows a slight increase for Cu_xO NWs-C/I compared to as-prepared Cu_xO NWs (Fig. S10 in the ESM). The highest O_A content in Cu_xO NWs-I facilitates the electrochemical reaction since O_A is believed to correlate with the active site of O-containing adsorption reactants [50]. Furthermore,

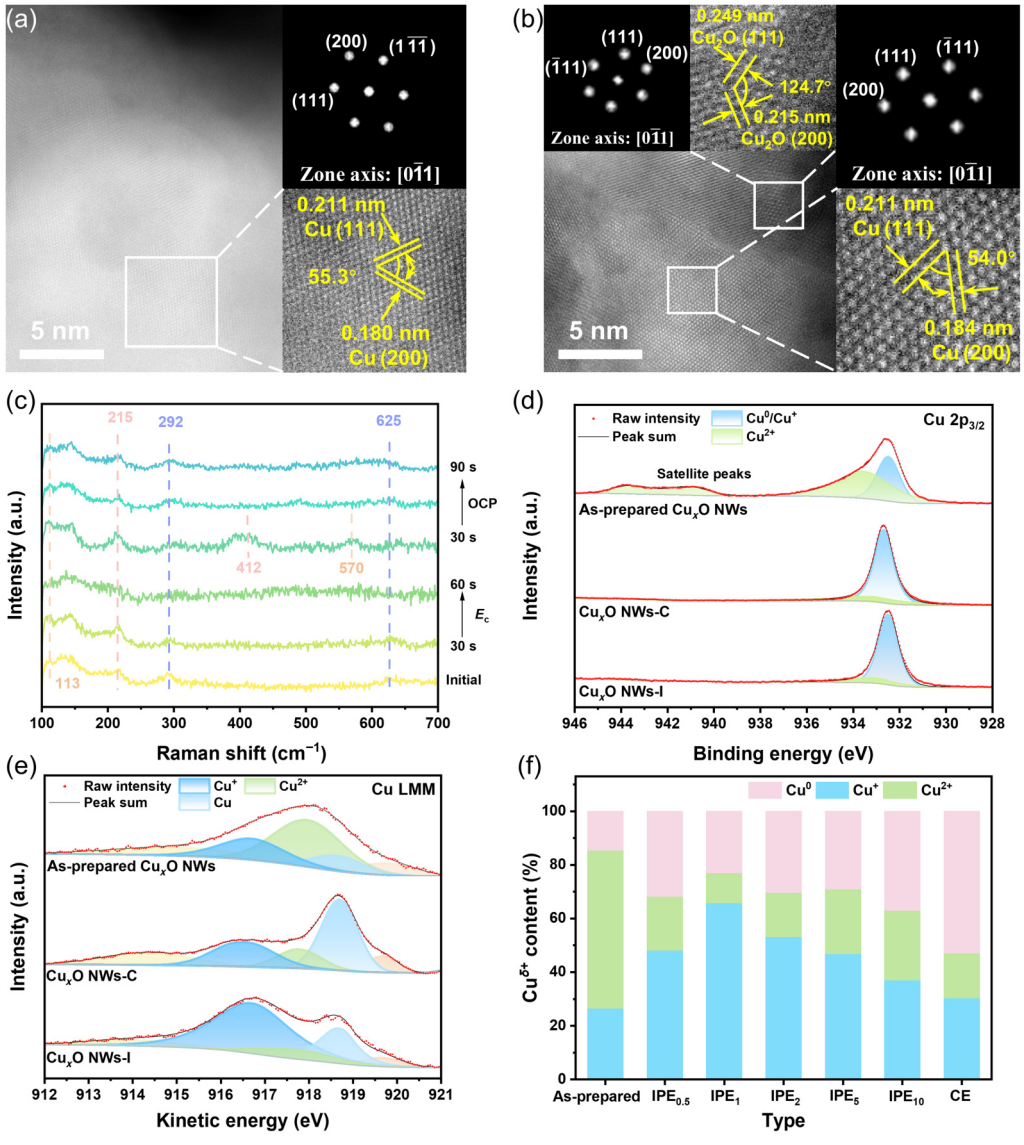

Figure 3 HAADF-STEM images of (a) Cu$_x$O NWs-C and (b) Cu$_x$O NWs-I. The insets in ((a) and (b)) show the details of white-squared regions and the corresponding filtered FFT patterns. (c) *In situ* Raman spectra of Cu$_x$O NWs at −0.5 V in the electrolyte containing 25 mM NO_2^-. (d) XPS spectra of Cu 2p and (e) AES spectra of Cu LMM for different Cu$_x$O NWs samples. (f) The content of Cu$^{\delta+}$ species for Cu$_x$O NWs under different conditions in the electrolyte with 25 mM NO_2^- (IPE$_{0.5-10}$ denotes t_c from 0.5 to 10 s under pulsed potential).

Auger electron spectroscopy (AES) is performed to distinguish Cu^0 from Cu$^+$ and to accurately determine the distribution of Cu$^{\delta+}$ species (Fig. 3(e)). The highest intensity peak of as-prepared Cu$_x$O NWs appears at 917.8 eV, where the most abundant Cu^{2+} content is about 59.0% [51]. The Cu LMM spectrum of Cu$_x$O NWs-C displays a characteristic peak at 918.7 eV, which is related to the generation of Cu^0 about 52.9% with a constant potential applied [52]. For Cu$_x$O NWs-I, the highest peak of 916.7 eV is observed, indicating Cu$^+$ species is dominant at approximately 65.8% [53]. The Cu LMM spectra of Cu$_x$O NWs following IPE with varying t_c are also characterized (Fig. S11 in the ESM). As illustrated in Fig. 3(f), the Cu$^+$ content exhibits a volcanic variation tendency with a gradual increase in t_c and the maximum Cu$^+$ content is observed at t_c = 1 s. Therefore, IPE is a facile approach to increase the content of advantageous Cu$^+$ species and improve the NH_3 synthesis performance of eNO_2RR.

It is also worth mentioning that applying potential in eNO_2RR induces subtle yet meaningful morphological changes in the Cu$_x$O NWs catalyst. Compared to the as-prepared Cu$_x$O NWs (Figs. 1(c)–1(e)), both CE and IPE modes lead to a transformation of the nanowires from upright to slightly curved configurations (Figs. S12 and S13 in the ESM). Meanwhile, the initially smooth surfaces become noticeably rougher, with fine cracks emerging after electrolysis. This roughening effect is more pronounced after IPE, suggesting that the intermittent reduction and oxidation of Cu$_x$O NWs generate a greater increase in active surface area than CE.

To assess the beneficial effects of the IPE mode, eNO_2RR performance evaluations are carried out at room temperature using an H-type electrolysis cell. The total duration of E_c for all pulsed experiments is controlled at 30 min to match the electrolysis time of the CE. Ultraviolet–visible (UV–Vis) spectrum is utilized to analyze both reductive products and reactants (Figs. S14 and S15 in the ESM) [54, 55]. First, linear sweep voltammetry (LSV) in 25 mM NO_2^- revealed that Cu foam requires more negative potentials to

achieve the same current density as Cu_xO NWs (Fig. S16 in the ESM), indicating that the latter exhibits more favorable eNO_2RR kinetics. Moreover, the Cu_xO NWs are superior to Cu foam in terms of NH_3 yield rate at both constant and intermittent pulsed potentials (Fig. S17 in the ESM).

Unless otherwise specified, the following tests utilize a consistent set of pulse parameters where $t_c = t_r = 1$ s. As shown in Fig. 4(a), the IPE mode achieves a substantially higher average current density (1227 mA·cm^{-2}) than CE mode (796 mA·cm^{-2}) during eNO_2RR at −0.7 V, indicating enhanced reaction kinetics. The influence of different NO_2^- concentrations on catalytic performance is further investigated using LSV curves (0 to 100 mM NO_2^-, Fig. S18 in the ESM). At low NO_2^- concentrations, CE suffers from intense competition with the HER, leading to a low FE and reduced NH_3 yield. Remarkably, the IPE mode mitigates this issue, providing a substantial performance enhancement (Fig. 4(b)) When NO_2^- concentration remains very low (at 5 mM), the FE increases from 28.99% (CE) to 52.07% (IPE), while at 10 mM, it rises from 44.12% to 71.61%. Meanwhile, the NH_3 yield rate of IPE mode (60.77 mg·h^{-1}·cm^{-2}) is 2.1 times higher than that of CE (28.42 mg·h^{-1}·cm^{-2}). Even at high NO_2^- concentrations (50 and 100 mM), where HER is partially suppressed, the IPE mode still outperforms CE mode due to the generation of more high-activity sites of Cu_2O (50 mM: 117.32 mg·h^{-1}·cm^{-2} for CE vs. 134.27 mg·h^{-1}·cm^{-2} for IPE; 100 mM: 148.46 mg·h^{-1}·cm^{-2} for CE vs. 165.83 mg·h^{-1}·cm^{-2} for IPE).

The catalytic activity of Cu_xO NWs is evaluated within the range of −0.4 to −0.8 V in the electrolyte with 25 mM NO_2^- (Fig. 4(c)). For the CE mode, the highest FE (92.78%) is achieved at −0.5 V, while the peak NH_3 yield rate (83.45 mg·h^{-1}·cm^{-2}) occurs at −0.6 V. In contrast, the IPE mode shows a maximum FE of 93.12% at −0.6 V and a highest NH_3 yield rate of 115.10 mg·h^{-1}·cm^{-2} at −0.7 V (FE = 91.14%). These values exceed those of CE and outperform many previously reported systems (Fig. 4(d) and Table S1 in the ESM). Competitive H_2 evolution was investigated by gas chromatography (GC), confirming HER is effectively suppressed by IPE mode, from 14.78% to 4.62% at −0.7 V (Fig. S19 in the ESM). While the total FE is less than 100%, indicating a portion of the current is allocated to catalyst reduction. Under IPE mode, catalyst reduction accounts for approximately 5%, while this proportion is less than 1% under CE mode, which suggests the majority of performance enhancement is attributed to accelerated NH_3 synthesis on abundant Cu_2O sites. To further verify HER suppression under IPE mode, online differential electrochemical mass spectrometry (DEMS) in 1 M NaOH + 25 mM $NaNO_2$ electrolyte was performed. As shown in Fig. 4(e), the intensity of H_2

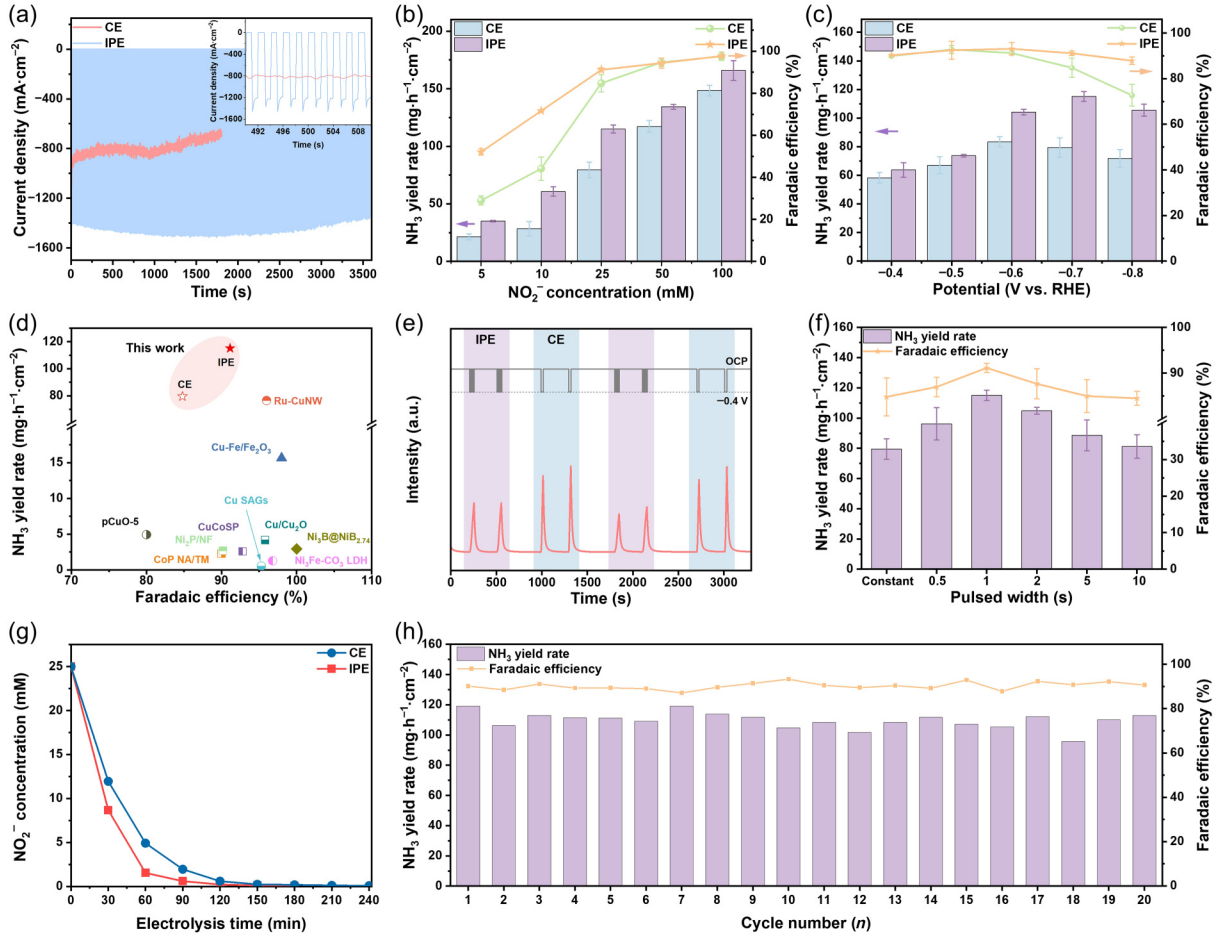

Figure 4 (a) Current density and the corresponding enlargement (inset) under CE and IPE ($t_r = t_c = 1$ s) mode. (b) Average NH_3 yield rate and FE in the electrolyte with different NO_2^- concentrations by CE (−0.7 V) and IPE ($t_r = t_c = 1$ s, $E_c = -0.7$ V). (c) Potential-dependent average NH_3 yield rate and FE over Cu_xO NWs in 25 mM NO_2^- ($t_r = t_c = 1$ s for pulsed potential). (d) Performance comparison of this work with previous reported studies. (e) Online DEMS of H_2 profiles ($m/z = 2$) for Cu_xO NWs in 25 mM NO_2^- with different electrolysis mode. (f) Effects of different t_c on NH_3 yield rate and FE in 25 mM NO_2^-. (g) NO_2^- removal by CE (−0.7 V) and IPE ($t_r = t_c = 1$ s, $E_c = -0.7$ V) in 25 mM NO_2^-. (h) Stability test of Cu_xO NWs under IPE mode at E_c of −0.7 V ($t_r = t_c = 1$ s, the total duration of each cycle for IPE is 1 h).

(m/z = 2) during IPE mode is obvious lower than that during CE mode. Additionally, the HER current density of CE and IPE modes are measured at various potentials in the electrolyte without NO_2^-, confirming that IPE can effectively inhibit HER for the Cu_xO NWs (Fig. S20 in the ESM). Besides, to probe the role of oxidation during IPE, Ar is introduced to exclude the air, since oxygen is one of the main contributors to reoxidizing $Cu^{\delta+}$ species. As a result, the current density and corresponding NH_3 yield rate of IPE are significantly reduced to the level of CE mode, which clearly implies the necessity of the re-oxidation process for performance enhancement (Fig. S21 in the ESM).

The t_c is an essential parameter for modulating IPE mode. The effect of t_c ($t_r = t_c$) on the catalytic behaviour of Cu_xO NWs catalyst is investigated under a fixed E_c of −0.7 V in the electrolyte containing 25 mM NO_2^-. The IPE mode under various t_c all shows better performance compared to CE (Fig. 4(f)). However, the NH_3 yield and FE follow a volcano-type trend with increasing t_c, peaking at 1 s. When t_c is prolonged to 10 s, the efficiency of NH_3 synthesis only slightly exceeds the CE mode. Furthermore, the trend of Cu^+ content with distinct t_c (Fig. 3(f)) is similar to that of catalytic performance, that is, the more Cu^+ in the Cu_xO NWs produced by the IPE, the higher NH_3 yield rate and FE attained. This finding reflects a crucial role of Cu^+ in eNO_2RR. Similarly, in 50 and 100 mM NO_2^- electrolyte, HER is partially suppressed. The catalytic performance at different t_c is comparable and IPE mode primarily enhances NH_3 yield via Cu^+ regeneration. However, the optimal t_c shifts to 0.5 s in low NO_2^- concentration (5 and 10 mM), where a shorter t_c is required to overcome severe diffusion limitations and competing HER. Thus, the IPE mode achieves significant higher NH_3 FE compared to CE mode (Fig. S22 in the ESM). These results demonstrate that the complex relationship between catalyst composition, pulse parameters and performance in eNO_2RR.

Long-term electrolysis reveals that IPE accelerates NO_2^- consumption. As shown in Fig. 4(g), IPE mode ($t_r = t_c$ = 1 s, E_c = −0.7 V) shortens the time required to reduce NO_2^- concentration to near-zero by ~ 25% compared to CE under identical conditions. As a result, the IPE mode over Cu_xO NWs is an efficient technique for decontaminating low NO_2^- concentrations in wastewater. The blank experiment is applied to verify that the NH_3 production comes only from the eNO_2RR process (Fig. S23 in the ESM). To ascertain the stability of Cu_xO NWs, recycle testing is conducted in IPE mode. Throughout up to 20 cycles (1 h each), the NH_3 yield rate and FE are relatively stable with no noticeable decay (Fig. 4(h) and Fig. S24 in the ESM). Meanwhile, SEM images show that the Cu_xO NWs maintain initial wire-like morphology after cyclic testing and are uniformly supported on the substrate, demonstrating the outstanding structural stability (Fig. S25 in the ESM).

4 Conclusions

In conclusion, we have successfully synthesized Cu_xO NWs catalyst and demonstrated their high performance in producing NH_3 via eNO_2RR under intermittent pulsed electrolysis. The highest NH_3 yield rate of 115.10 $mg \cdot h^{-1} \cdot cm^{-2}$ and FE of 91.14% were achieved in 25 mM NO_2^- electrolyte. The pulsed switching between the OCP and cathodic potentials stabilizes the Cu_2O phase while suppressing metallic Cu^0 formation. Consistent with theoretical predictions, Cu_2O demonstrates enhanced NO_2^- adsorption and suppressed HER activity, leading to improved performance. This work provides an efficient approach to stabilize the catalytically favorable Cu_2O active phase and improve NH_3 selectivity, particularly under low NO_2^- concentrations, offering valuable insights for the development of efficient and selective eNO_2RR systems.

Electronic Supplementary Material: Supplementary material (chemicals and material, synthesis of Cu_xO NWs, detailed experimental procedures, and addition information about TEM, XRD, XPS, Raman, and DFT calculations) is available in the online version of this article at https://doi.org/10.26599/NR.2025.94907810.

Data availability

All data needed to support the conclusions in the paper are presented in the manuscript and the Electronic Supplementary Material. Additional data related to this paper may be requested from the corresponding author upon request.

Acknowledgements

This work was financially supported in part by the National Key R&D Program of China (No. 2024YFA1509400), the National Natural Science Foundation of China (No. 52302094), and Natural Science Foundation of Jiangxi, China (No. 20232ACB203002).

Declaration of competing interest

All the contributing authors report no conflict of interests in this work.

Author contribution statement

Z. M.: Data curation, validation, writing manuscript, experimental design. J.-H. Y.: Data curation, writing manuscript, validation. Y.-T. Z.: Experimental design, writing manuscript. X.-F. S.: Validation. X.-L. H.: Project administration, funding acquisition, revising manuscript. M.-M. S.: Validation. F.-F. Z.: Validation, revising manuscript. J.-M. Y.: Project administration, funding acquisition, review. Q. J.: Review. All the authors have approved the final manuscript.

Use of AI statement

None.

References

[1] Erisman, J. W.; Sutton, M. A.; Galloway, J.; Klimont, Z.; Winiwarter, W. How a century of ammonia synthesis changed the world. *Nat. Geosci.* **2008**, *1*, 636–639.

[2] Suryanto, B. H. R.; Du, H. L.; Wang, D. B.; Chen, J.; Simonov, A. N.; MacFarlane, D. R. Challenges and prospects in the catalysis of electroreduction of nitrogen to ammonia. *Nat. Catal.* **2019**, *2*, 290–296.

[3] Chen, J. G.; Crooks, R. M.; Seefeldt, L. C.; Bren, K. L.; Bullock, R. M.; Darensbourg, M. Y.; Holland, P. L.; Hoffman, B.; Janik, M. J.; Jones, A. K. et al. Beyond fossil fuel-driven nitrogen transformations. *Science* **2018**, *360*, eaar6611.

[4] van der Ham, C. J. M.; Koper, M. T. M.; Hetterscheid, D. G. H. Challenges in reduction of dinitrogen by proton and electron transfer. *Chem. Soc. Rev.* **2014**, *43*, 5183–5191.

[5] Tang, C.; Qiao, S. Z. How to explore ambient electrocatalytic nitrogen

reduction reliably and insightfully. *Chem. Soc. Rev.* **2019**, *48*, 3166–3180.
[6] Guo, W. H.; Zhang, K. X.; Liang, Z. B.; Zou, R. Q.; Xu, Q. Electrochemical nitrogen fixation and utilization: Theories, advanced catalyst materials and system design. *Chem. Soc. Rev.* **2019**, *48*, 5658–5716.
[7] Bao, D.; Zhang, Q.; Meng, F. L.; Zhong, H. X.; Shi, M. M.; Zhang, Y.; Yan, J. M.; Jiang, Q.; Zhang, X. B. Electrochemical reduction of N_2 under ambient conditions for artificial N_2 fixation and renewable energy storage using N_2/NH_3 cycle. *Adv. Mater.* **2017**, *29*, 1604799.
[8] Yue, L. C.; Song, W.; Zhang, L. X.; Luo, Y. L.; Wang, Y.; Li, T. S.; Ying, B. W.; Sun, S. J.; Zheng, D. D.; Liu, Q. et al. Recent advance in heterogenous electrocatalysts for highly selective nitrite reduction to ammonia under ambient condition. *Small Struct.* **2023**, *4*, 2300168.
[9] Wang, J.; Feng, T.; Chen, J. X.; Ramalingam, V.; Li, Z. X.; Kabtamu, D. M.; He, J. H.; Fang, X. S. Electrocatalytic nitrate/nitrite reduction to ammonia synthesis using metal nanocatalysts and bio-inspired metalloenzymes. *Nano Energy* **2021**, *86*, 106088.
[10] Camargo, J. A.; Alonso, Á. Ecological and toxicological effects of inorganic nitrogen pollution in aquatic ecosystems: A global assessment. *Environ. Int.* **2006**, *32*, 831–849.
[11] Jensen, F. B. Nitrite disrupts multiple physiological functions in aquatic animals. *Comp. Biochem. Physiol. Part A: Mol. Integr. Physiol.* **2003**, *135*, 9–24.
[12] Zhao, D. L.; Liang, J.; Li, J.; Zhang, L. C.; Dong, K.; Yue, L. C.; Luo, Y. S.; Ren, Y. C.; Liu, Q.; Hamdy, M. S. et al. A TiO_{2-x} nanobelt array with oxygen vacancies: An efficient electrocatalyst toward nitrite conversion to ammonia. *Chem. Commun.* **2022**, *58*, 3669–3672.
[13] Chen, Q. Y.; An, X. G.; Liu, Q.; Wu, X. Q.; Xie, L. S.; Zhang, J.; Yao, W. T.; Hamdy, M. S.; Kong, Q. Q.; Sun, X. P. Boosting electrochemical nitrite-ammonia conversion properties by a Cu foam@Cu_2O catalyst. *Chem. Commun.* **2022**, *58*, 517–520.
[14] Gao, R.; Dai, T. Y.; Meng, Z.; Sun, X. F.; Liu, D. X.; Shi, M. M.; Li, H. R.; Kang, X.; Bi, B.; Zhang, Y. T. et al. A bifunctional catalyst for green ammonia synthesis from ubiquitous air and water. *Adv. Mater.* **2023**, *35*, 2303455.
[15] Meng, Z.; Yao, J. X.; Sun, C. N.; Kang, X.; Gao, R.; Li, H. R.; Bi, B.; Zhu, Y. F.; Yan, J. M.; Jiang, Q. Efficient ammonia production beginning from enhanced air activation. *Adv. Energy Mater.* **2022**, *12*, 2202105.
[16] Katsounaros, I.; Dortsiou, M.; Kyriacou, G. Electrochemical reduction of nitrate and nitrite in simulated liquid nuclear wastes. *J. Hazard. Mater.* **2009**, *171*, 323–327.
[17] Zhang, B. C.; Dai, Z. C.; Chen, Y. X.; Cheng, M. Y.; Zhang, H. K.; Feng, P. Y.; Ke, B. Q.; Zhang, Y. Y.; Zhang, G. Q. Defect-induced triple synergistic modulation in copper for superior electrochemical ammonia production across broad nitrate concentrations. *Nat. Commun.* **2024**, *15*, 2816.
[18] Yu, L. Y.; Zhang, X. S.; Xiao, K.; Yu, L.; Cao, F. M.; Zhao, H. H.; Sun, J.; Yang, Y. J. On-line determination of nitrite in tannery effluent by reverse reference flow injection. *J. Soc. Leather Technol. Chem.* **2010**, *94*, 124–128.
[19] Klevinskas, A.; Kantminienė, K.; Žmuidzinavičienė, N.; Jonuškienė, I.; Griškonis, E. Microbial fuel cell as a bioelectrochemical sensor of nitrite ions. *Processes.* **2021**, *9*, 1330.
[20] Zhao, J.; Shen, Z.; Yu, J.; Guo, Y.; Mushtaq, M. A.; Ding, Y. B.; Song, Z. Q.; Zhang, W.; Huang, X.; Li, Y. et al. Constructing Cu–CuO heterostructured skin on Cu cubes to promote electrocatalytic ammonia production from nitrate wastewater. *J. Hazard. Mater.* **2022**, *439*, 129653.
[21] Yang, P. P.; Zhang, X. L.; Gao, F. Y.; Zheng, Y. R.; Niu, Z. Z.; Yu, X. X.; Liu, R.; Wu, Z. Z.; Qin, S.; Chi, L. P. et al. Protecting copper oxidation state via intermediate confinement for selective CO_2 electroreduction to C_{2+} fuels. *J. Am. Chem. Soc.* **2020**, *142*, 6400–6408.
[22] Xin, S. S.; Shen, J. G.; Liu, G. C.; Chen, Q. H.; Xiao, Z.; Zhang, G. D.; Xin, Y. J. Electricity generation and microbial community of single-chamber microbial fuel cells in response to Cu_2O nanoparticles/reduced graphene oxide as cathode catalyst. *Chem. Eng. J.* **2020**, *380*, 122446.
[23] Gong, Z. H.; Zhong, W. Y.; He, Z. Y.; Liu, Q. Y.; Chen, H. J.; Zhou, D.; Zhang, N. A.; Kang, X. W.; Chen, Y. Regulating surface oxygen species on copper(I) oxides via plasma treatment for effective reduction of nitrate to ammonia. *Appl. Catal. B: Environ.* **2022**, *305*, 121021.
[24] Chen, G. F.; Yuan, Y. F.; Jiang, H. F.; Ren, S. Y.; Ding, L. X.; Ma, L.; Wu, T. P.; Lu, J.; Wang, H. H. Electrochemical reduction of nitrate to ammonia via direct eight-electron transfer using a copper-molecular solid catalyst. *Nat. Energy* **2020**, *5*, 605–613.
[25] Yan, Q. Y.; Zhao, R. D.; Yu, L. H.; Zhao, Z. Y.; Liu, L.; Xi, J. Y. Enhancing compatibility of two-step tandem catalytic nitrate reduction to ammonia over P–Cu/$Co(OH)_2$. *Adv. Mater.* **2024**, *36*, 2408680.
[26] Zhao, R. D.; Yan, Q. Y.; Yu, L. H.; Yan, T.; Zhu, X. Y.; Zhao, Z. Y.; Liu, L.; Xi, J. Y. A Bi–Co Corridor construction effectively improving the selectivity of electrocatalytic nitrate reduction toward ammonia by nearly 100%. *Adv. Mater.* **2023**, *35*, 2306633.
[27] Zhao, R. D.; Yan, Q. Y.; Lu, L.; Yu, L. H.; Chen, H.; Yan, T.; Liu, L.; Xi, J. Y. Nitrite-mediated pulsed electrocatalytic nitrate reduction to ammonia over Co@Cu NW with dual active sites. *ACS Catal.* **2024**, *14*, 17046–17054.
[28] Wang, Y. T.; Zhou, W.; Jia, R. R.; Yu, Y. F.; Zhang, B. Unveiling the activity origin of a copper-based electrocatalyst for selective nitrate reduction to ammonia. *Angew. Chem., Int. Ed.* **2020**, *59*, 5350–5354.
[29] Liang, J.; Li, Z. X.; Zhang, L. C.; He, X.; Luo, Y. S.; Zheng, D. D.; Wang, Y.; Li, T. S.; Yan, H.; Ying, B. W. et al. Advances in ammonia electrosynthesis from ambient nitrate/nitrite reduction. *Chem* **2023**, *9*, 1768–1827.
[30] Dai, L.; Qin, Q.; Wang, P.; Zhao, X. J.; Hu, C. Y.; Liu, P. X.; Qin, R. X.; Chen, M.; Ou, D. H.; Xu, C. F. et al. Ultrastable atomic copper nanosheets for selective electrochemical reduction of carbon dioxide. *Sci. Adv.* **2017**, *3*, e1701069.
[31] Qiu, W. X.; Wang, P. F.; Jin, Z. Y.; Liu, W.; Li, P. P.; Pan, Z. C. Pulsed photoelectrocatalysis-mediated reactive chlorine spillover promotes nanoconfined cascade denitrification. *Appl. Catal. B: Environ. Energy* **2025**, *367*, 125102.
[32] Li, P. P.; Li, R.; Liu, Y. T.; Xie, M. H.; Jin, Z. Y.; Yu, G. H. Pulsed nitrate-to-ammonia electroreduction facilitated by tandem catalysis of nitrite intermediates. *J. Am. Chem. Soc.* **2023**, *145*, 6471–6479.
[33] Arán-Ais, R. M.; Scholten, F.; Kunze, S.; Rizo, R.; Roldan Cuenya, B. The role of *in situ* generated morphological motifs and Cu(I) species in C_{2+} product selectivity during CO_2 pulsed electroreduction. *Nat. Energy* **2020**, *5*, 317–325.
[34] Bui, J. C.; Kim, C.; Weber, A. Z.; Bell, A. T. Dynamic boundary layer simulation of pulsed CO_2 electrolysis on a copper catalyst. *ACS Energy Lett.* **2021**, *6*, 1181–1188.
[35] Dong, X. R.; Fang, Z. X.; Gu, Y.; Zhou, X. G.; Tian, C. G. Two-dimensional porous Cu–CuO nanosheets: Integration of heterojunction and morphology engineering to achieve high-effective and stable reduction of the aromatic nitro-compounds. *Chin. Chem. Lett.* **2023**, *34*, 107295.
[36] Wang, H.; Luo, Y. Y.; Liu, B.; Gao, L.; Duan, G. T. CuO Nanoparticle loaded ZnO hierarchical heterostructure to boost H_2S sensing with fast recovery. *Sens. Actuators B: Chem.* **2021**, *338*, 129806.
[37] Nørskov, J. K.; Bligaard, T.; Rossmeisl, J.; Christensen, C. H. Towards the computational design of solid catalysts. *Nat. Chem.* **2009**, *1*, 37–46.
[38] Zhou, N.; Wang, Z.; Zhang, N.; Bao, D.; Zhong, H. X.; Zhang, X. B. Potential-induced synthesis and structural identification of oxide-derived Cu electrocatalysts for selective nitrate reduction to ammonia. *ACS Catal.* **2023**, *13*, 7529–7537.

[39] Huang, X. L.; Wang, F. H.; Ma, L. P.; Wang, J. W.; Zhang, T. Y.; Hao, X. Y.; Chi, X.; Cheng, H.; Yang, M.; Ding, J. et al. Reversion of catalyst valence states for highly efficient water oxidation. *Catal. Sci. Technol.* **2023**, *13*, 2820–2826.

[40] Fu, Y. F.; Wang, S.; Wang, Y.; Wei, P. F.; Shao, J. Q.; Liu, T. F.; Wang, G. X.; Bao, X. H. Enhancing electrochemical nitrate reduction to ammonia over Cu nanosheets via facet tandem catalysis. *Angew. Chem., Int. Ed.* **2023**, *62*, e202303327.

[41] Kim, C.; Cho, K. M.; Park, K.; Kim, J. Y.; Yun, G. T.; Toma, F. M.; Gereige, I.; Jung, H. T. Cu/Cu_2O interconnected porous aerogel catalyst for highly productive electrosynthesis of ethanol from CO_2. *Adv. Funct. Mater.* **2021**, *31*, 2102142.

[42] Debbichi, L.; de Lucas, M. C. M.; Pierson, J. F.; Krüger, P. Vibrational properties of CuO and Cu_4O_3 from first-principles calculations, and raman and infrared spectroscopy. *J. Phys. Chem. C* **2012**, *116*, 10232–10237.

[43] Deng, Y. L.; Handoko, A. D.; Du, Y. H.; Xi, S. B.; Yeo, B. S. *In situ* Raman spectroscopy of copper and copper oxide surfaces during electrochemical oxygen evolution reaction: Identification of Cu^{III} oxides as catalytically active species. *ACS Catal.* **2016**, *6*, 2473–2481.

[44] Lim, M.; Sun, J.; Ma, Z. P.; Jalili, R.; Daiyan, R.; Lovell, E. C.; Amal, R. Engineering CuO_x nanoparticles on Cu foam for acidic nitrate reduction to ammonium. *ACS Appl. Nano Mater.* **2023**, *6*, 4936–4945.

[45] Singhal, A.; Pai, M. R.; Rao, R.; Pillai, K. T.; Lieberwirth, I.; Tyagi, A. K. Copper(I) oxide nanocrystals-one step synthesis, characterization, formation mechanism, and photocatalytic properties. *Eur. J. Inorg. Chem.* **2013**, *2013*, 2640–2651.

[46] Zhang, J. Y.; Guo, B.; Liang, J.; Zou, L.; Lu, J.; Liu, J. X. Au-doped CuO_x nanoparticles as electrocatalysts for oxygen evolution reaction. *ACS Appl. Nano Mater.* **2022**, *5*, 6500–6504.

[47] Bodappa, N.; Su, M.; Zhao, Y.; Le, J. B.; Yang, W. M.; Radjenovic, P.; Dong, J. C.; Cheng, J.; Tian, Z. Q.; Li, J. F. Early stages of electrochemical oxidation of Cu(111) and polycrystalline Cu surfaces revealed by *in situ* Raman spectroscopy. *J. Am. Chem. Soc.* **2019**, *141*, 12192–12196.

[48] Wang, M.; Shen, M.; Jin, X. X.; Tian, J. J.; Li, M. L.; Zhou, Y. J.; Zhang, L. X.; Li, Y. S.; Shi, J. L. Oxygen vacancy generation and stabilization in CeO_{2-x} by Cu introduction with improved CO_2 photocatalytic reduction activity. *ACS Catal.* **2019**, *9*, 4573–4581.

[49] Chang, F. F.; Liu, Y. P.; Wei, J. C.; Yang, L.; Bai, Z. Y. *In situ* surface/interface generation on Cu_2O nanostructures toward enhanced electrocatalytic CO_2 reduction to ethylene using *operando* spectroscopy. *Inorg. Chem. Front.* **2023**, *10*, 240–249.

[50] Xu, Y.; Ren, K. L.; Ren, T. L.; Wang, M. Z.; Wang, Z. Q.; Li, X. N.; Wang, L.; Wang, H. J. Ultralow-content Pd *in-situ* incorporation mediated hierarchical defects in corner-etched Cu_2O octahedra for enhanced electrocatalytic nitrate reduction to ammonia. *Appl. Catal. B: Environ.* **2022**, *306*, 121094.

[51] Sung, M. M.; Sung, K.; Kim, C. G.; Lee, S. S.; Kim, Y. Self-assembled monolayers of alkanethiols on oxidized copper surfaces. *J. Phys. Chem. B* **2000**, *104*, 2273–2277.

[52] Wei, C. H. N.; Wu, G. X.; Yang, S. J.; Liu, Q. M. Electrochemical deposition of layered copper thin films based on the diffusion limited aggregation. *Sci. Rep.* **2016**, *6*, 34779.

[53] Peng, C. K.; Lin, Y. C.; Chiang, C. L.; Qian, Z. X.; Huang, Y. C.; Dong, C. L.; Li, J. F.; Chen, C. T.; Hu, Z. W.; Chen, S. Y. et al. Zhang-rice singlets state formed by two-step oxidation for triggering water oxidation under *operando* conditions. *Nat. Commun.* **2023**, *14*, 529.

[54] Shi, M. M.; Bao, D.; Wulan, B. R.; Li, Y. H.; Zhang, Y. F.; Yan, J. M.; Jiang, Q. Au Sub-Nanoclusters on TiO_2 toward highly efficient and selective electrocatalyst for N_2 conversion to NH_3 at ambient conditions. *Adv. Mater.* **2017**, *29*, 1606550.

[55] Li, L. Q.; Tang, C.; Cui, X. Y.; Zheng, Y.; Wang, X. S.; Xu, H. L.; Zhang, S.; Shao, T.; Davey, K.; Qiao, S. Z. Efficient nitrogen fixation to ammonia through integration of plasma oxidation with electrocatalytic reduction. *Angew. Chem., Int. Ed.* **2021**, *60*, 14131–14137.